On the Accuracy of Equivalent Antenna Representations – A Case Study

Johan Malmström, Henrik Holter, and B. L. G. Jonsson

Abstract—
The accuracy of two equivalent antenna representations, near-field sources and far-field sources, are evaluated for an antenna installed on a simplified platform. We show that the accuracy of the installed far-field and surface current for the investigated weakly scattering platform, depends strongly on the configurations associated with the equivalent antenna representation. The root-mean-square error for the installed far-field error vary between $4.4\% - 8.4\%$ for the considered configurations of near field equivalent representations installed on the investigated platform. When using far-field sources, the design parameters have an even larger influence of the achieved accuracy. There is also a varying accuracy depending on the type of numerical method used. Based on the results, some recommendations on the choice of sub-domain for the equivalent antenna representation are given associated with the platform. In industrial antenna applications, the accuracy in determining e.g. installed far-fields and antenna isolation on large platforms are critical. Equivalent representations can reduce the fine-detail complexity of antennas and thus give an efficient numerical descriptions to be used in large-scale simulations. The results in this paper highlights to antenna designers and system engineers the accuracy challenges associated with the use of equivalent antenna representations.

Index Terms—Antenna modeling, Computational electromagnetics, Electromagnetic analysis, Electromagnetic modeling.

I. INTRODUCTION

THE INCREASING accuracy of full-wave large-scale simulation of complex electromagnetic (EM) problems has changed the industrial design-process of radio frequency (RF) systems. The construction of scaled models for measurements has widely been replaced by simulations. This work flow saves both time and money as compared to building prototypes for measurements [1]. For simulations to be trustworthy, in particular in industrial design processes, an a-priori predictable accuracy is essential.

The reason for the large interest in simulations within the electromagnetic community is that electromagnetic scattering problems are rarely possible to solve analytically. Problems involving realistic antennas are therefore usually solved numerically. For small-scale systems, a detailed model of the physical antenna serves as a good model for accurately determining associated fields, impedances, and currents with numerical methods. This is documented by e.g. the annual benchmarks given by the EurAAP working group on software [2], where different simulation methods and measurements are compared [3]. Increasing agreement over the last few years between simulations and measurements has been reported [4]. For electrically large platforms, it is problematic to include models of the antenna and the complete platform in the same simulation, since the computational time and memory requirement grow with the electrical size [5].

Simulations of electrically large platforms in combination with complex antennas, can lead to extreme computational time and memory requirement. In these cases, a less complex antenna model can significantly reduce the overall complexity of the simulation. Using an equivalent representation of the antenna is one way to reduce the complexity of the antenna model. An equivalent antenna representation also opens the possibility to utilize different numerical methods in different parts of the simulation domain, sometimes referred to as a hybrid method.

On large platforms, special techniques can be used to reduce memory requirements, e.g. asymptotic methods (physical optics or geometrical optics), or domain decomposition methods (DDM). In DDM, a large simulation is split into several smaller sub-problems that are solved in parallel [6]. It has been used in e.g. [7–10]. A drawback with domain decomposition is that the complexity is increased as compared to a full-domain simulation, since information has to be exchanged over the interface between adjacent sub-domains.

One way of decomposing a large EM problem is to analyze the antennas in isolation, and imprint the results in the platform model. In a basic domain decomposition, multiple scattering effects between structures in different domains are neglected, which implies that there is no need for iterations over the interface between adjacent sub-domains. In that case, the sub-domain with the antenna serves as an equivalent representation of the antenna, in the same way as in this work. When installing antennas on a platform, the antennas are often placed so that the scattering on the platform is low. In those cases, it is a minor approximation to neglect multiple scattering over the interface.

Source modeling in electromagnetics has been of scientific interest for a long time, where major contributions have been made by e.g. Hallén, King and Harrington. Some of these works are reviewed in e.g. [16]. These classical works focus mainly on antenna excitations for a specific type of antenna, e.g. wire antennas. The two here studied equivalent representations, near-fields sources and far-field sources, are general in the sense that they can be used to represent any type of antenna. The underlying theories for these two representations, the equivalence principle and far-field pattern generation, are both described in literature; see e.g. [17] and the references within. They are also implemented in several commercial

J. Malmström and H. Holter are with Saab Surveillance, Stockholm, Sweden. B. L. G. Jonsson is with the Electromagnetic Engineering Laboratory, KTH Royal Institute of Technology, Stockholm, Sweden.

software, see e.g. [11], [13]. Results from using equivalent representations are described in several articles, e.g. [10], [18–21], where near-field sources are used, and e.g. [22] that shows examples when using far-field sources.

Commercial software for computational electromagnetics (CEM), see e.g. [11–14], and recommendations for using CEM has been thoroughly discussed in the literature see e.g. [15]. From an industrial perspective it is of major interest to get a highly accurate solution, but equally important to get a predictable accuracy. Equivalent antenna representations are becoming more important tool in EM-simulations. Software documentation can give designers valuable rule-of-thumb recommendations about preferred configurations of equivalent antenna representation, but the recommendations seldom give any information about the expected accuracy when using the equivalent representation on platforms. Unfortunately, it is not obvious which configuration of the equivalent antenna representation that is most accurate or how large error the equivalent antenna representation introduce.

In this paper we make a first effort to investigate accuracy errors associated with using equivalent antenna representations for antennas installed on platforms. To emphasize the dependence of the parameters and geometries associated with the equivalent antenna representations, we consider one small and low-scattering platform. Different equivalent antenna representations are tested on this platform.

The accuracy of two key antenna parameters are investigated: the installed far-field, which is one of the most important characteristic of an installed antenna, and the induced surface current on the platform, which is important in both EMC applications and in antenna placement studies [1].

This study illustrate the sensitivity of the far-field and surface currents with respect to different equivalent antenna representations, as well as for different parameter configurations and different numerical methods. We show that the remnant part of the platform used when the equivalent representation of the installed antenna is determined strongly influence the accuracy. The results of the paper indicate what order of magnitudes of errors that equivalent antenna models introduce for the given platform. Even though it is non-trivial to translate these errors to other platforms, an essential result of this study is to demonstrate the need for accuracy studies in the use of equivalent antenna representations for platform installed antennas.

The paper consists of the following sections. Section II describe the theory used in the article and Section III the used methods and models. The results are presented in Section IV. We evaluate the accuracy of near-field sources in Section IV-B, far-field sources in Section IV-C, and their combination with different numerical methods in Section IV-D. The paper ends with a discussion and conclusions in Section V.

II. EQUIVALENCE THEORY

Two types of equivalent antenna representations are evaluated in this paper; near-field sources and far-field sources. Both representations are applicable to any kind of antenna or radiating structure.

A. Near-field Sources

The equivalence principle, introduced by Love [23] and refined by Schelkunoff [24], implies that any radiating structure can be represented by electric J and magnetic M surface currents on a fictitious surface Γ_e enclosing the radiating structure [25]. If the material outside Γ_e is homogeneous, it can be deduced that J and M reproduce exactly the same electric and magnetic fields outside Γ_e as the original antenna, whereas the fields inside Γ_e are zero [25], [26]. A near-field source (NFS) is the set of surface currents J, M on the surface Γ_e, a *Huygens' surface*. With the presence of a platform, the homogeneous requirement is not fulfilled and the near-field source only reproduces the original fields approximately.

The surface currents J and M, which we hereafter refer to as *currents*, are directly related to the discontinuity of the tangential electric and magnetic fields on the surface Γ_e. Since the currents J, M produce zero fields inside the surface Γ_e, the currents on Γ_e can be written as [25], [27]

$$J = \hat{\mathbf{n}} \times H, \tag{1}$$
$$M = -\hat{\mathbf{n}} \times E, \tag{2}$$

where E and H are the electric and magnetic fields on Γ_e and $\hat{\mathbf{n}}$ is the outward pointing normal to the surface Γ_e.

It can be beneficial to use a near-field representation of an antenna instead of a model of the physical antenna. One reason is if the number of mesh cells in the model including the platform decreases. Also, it opens up for using different numerical methods when analyzing the antenna and the platform.

When an antenna is installed on a platform, the surrounding material is non-homogeneous; the platform is typically made of conducting or dielectric material that is surrounded by e.g. air or vacuum. Using a near-field source to represent the antenna in a situation when the homogeneous condition is violated introduces an error because the surface currents are not correctly described. Hence, using a near-field source under this common circumstance is an approximation. The error from this approximation is effected by the choice of sub-domain.

B. Far-field Sources

Antenna radiation patterns are commonly used to characterize antennas. They describes magnitude, phase and polarization of the propagating waves generated by the antenna, for directions φ, θ, and a fixed distance r. The *far-field radiation pattern* is the leading order behavior as $r \to \infty$ [25].

A far-field radiation pattern can be used as an equivalent source in electromagnetic simulations. We will then refer to it as a far-field source (FFS). For reciprocal antennas, it also describes the receiving characteristics of the antenna. The far-field source is characterized by its far-field radiation pattern imposed as an infinitesimally small source at a given position. This position, together with the approximation of the platform when generating the far-field source, are the design parameters for far-field sources. Their impact on the accuracy of the solution is non-trivial, and is examined in Section IV-C.

Far-field sources are, compared to near-field sources, more a primitive representation, and are not expected to perform as
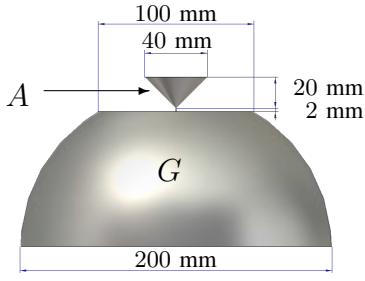
Fig. 1. The platform geometry G with the mono-cone antenna A placed on its flat top.

Fig. 2. Calculation domains: (a) The full domain D_0 is used when solving the reference case, (b) the sub-domain D_1 is used when generating the equivalent sources. The domain D_0 is used for imprinting the equivalent sources, (c) near-field sources on the interface Γ_e and (d) point-shaped far-field sources placed a distance h above the flat platform top surface.

good. On the contrary, they provide very efficient representations in numerical methods, from an implementation point of view. The error introduced by the far-field approximation is small when the far-field source is far from surrounding structure, e.g. a horn antenna feeding a parabolic reflector, see e.g. [28]. However, far-field sources have be used also near structures, see e.g. [22].

A far-field can be represented with spherical wave expansion (SWE) [27]. Such an expansion can increase the accuracy close to the source point, i.e. in the near field region. However, with a far-field source installed on a platform, SWE cannot be used, since it requires that there is no charge or current carrying structure within a certain distance from the center point of the expansion [27]. Therefore, SWE is not further considered in this paper.

Using a far-field source, its emitted radiation will locally be a plane wave, irrespective of the true distance between the far-field source and an evaluation point. A far-field source can be used e.g. in an integral equation formulation, where the point source is used as a field source within the computation domain. Implementation details of the point-shaped far-field source depend on the type of numerical method used, see e.g. [5], [29], [30] for general discussions.

III. METHODS

We use a series of case studies to investigate the accuracy of equivalent antenna representations for different configurations in the presence of a platform. For electromagnetic problems, where analytic solutions can rarely be found, the case study is an effective tool to compare configurations.

A. Geometrical Model

We choose here a platform geometry G and an antenna A.

The platform geometry G should have a simple and well defined shape, but still retain platform specific features. The chosen platform geometry G is depicted in Fig. 1. The geometry is a cut 200 mm diameter half-sphere, where the top diameter is 100 mm. It is perfectly electrically conducting (PEC). The geometry G is of electrical size of about 7λ at 10 GHz and has the following platform like properties:

- Finite support of surface currents,
- weak back-scattering from its edges to the antenna,
- radiating creeping waves on the curved surface.

The antenna A is a mono-cone antenna, also depicted in Fig. 1, with 20 mm top radius and 20 mm height. The antenna
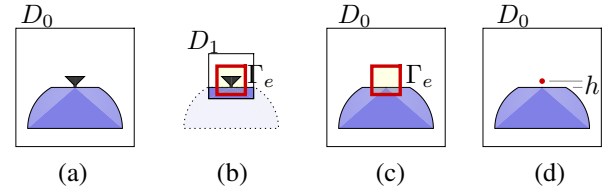
is mounted centrally on the flat top surface of the platform with a 2 mm feed gap. It is fed with a wave-guide port via a 10 mm long coaxial cable. A mono-cone antenna has an isolated far-field radiation pattern similar to a mono-pole but is more wideband.

We are interested in determining fields and currents in the domain on and outside the geometries $G \cup A$. Both the main geometry G and the mono-cone antenna A are rotational symmetric, implying that fields and currents will have the same symmetry. Hence, it is sufficient to evaluate these quantities at a fixed azimuth φ.

B. Calculation Domains

For usage in the rest of this paper, the following domain, as in Fig. 2, are defined:

- The domain D_0 that contain the platform geometry G and the antenna A.
- A sub-domain D_1 that contain the antenna and a selected part of the platform. As the equivalent source is intended to improve calculation time and memory use, the sub-domain D_1 should be much smaller than the domain D_0.
- A Huygens' surface Γ_e, i.e. a fictitious surface enclosing the antenna. The Huygens' surface Γ_e is completely included in the sub-domain D_1.

In a platform specific problem, e.g. with aircraft or ships, the domain D_0 is often electrically very large. However, a comparatively small domain D_0 is used in this work, which allows us to obtain a highly accurate reference solution for the fields and currents that is subsequently used in our benchmarks. The equivalent sources can be used on electrically large structures as well, so the methods and observations are applicable to antennas on e.g. ships or aircraft.

An antenna induces currents on surrounding structures. Such currents also contribute to the equivalent source. By using a smaller platform approximation domain D_1 to determine the equivalent sources, we implicitly ignore currents outside D_1. The larger part of the platform that is included in the platform approximation domain D_1, the smaller the error will be, but the computational cost to determine the equivalent source increases with growing size of D_1.

1) Work Flow for Using an Equivalent Near-field Source:

- In the sub-domain D_1; Calculate the tangential electric and magnetic fields, $\hat{\mathbf{n}} \times \boldsymbol{E}$ and $\hat{\mathbf{n}} \times \boldsymbol{H}$, on the surface Γ_e generated by the antenna, see Fig. 2(b).

- In the domain D_0; Remove the model of the physical antenna[1] and imprint the equivalent currents $\boldsymbol{J} = \hat{\mathbf{n}} \times \boldsymbol{H}$ and $\boldsymbol{M} = -\hat{\mathbf{n}} \times \boldsymbol{E}$ on Γ_e, see Fig. 2(c).
- Determine the fields in the domain D_0 using $\boldsymbol{J}$, $\boldsymbol{M}$ as equivalent sources.

We use a rectangular box as surface Γ_e for the equivalent currents that define the near-fields source.

2) Work Flow for Using an Equivalent Far-field Source:

- In the sub-domain D_1; Calculate the far-field radiation pattern generated by the antenna, see Fig. 2(b). This is the equivalent far-field source.
- Choose a height h over the main geometry where the far-field source is imprinted.
- In the domain D_0; Remove the model of the physical antenna and determine the fields using the far-field source, see Fig. 2(d).

The procedures described above in III-B1–III-B2 is general and applies to any kind of structure, not only the platform and the antenna used in this case study.

C. Evaluation

The results in e.g. [2–4] indicate that full-wave simulation results can be used as a benchmark of antenna behavior. We evaluate the electric current and the installed far-field pattern by comparing simulations with equivalent antenna representations against an accurate reference solution using a model with the physical antenna.

When comparing results from simulations, one must keep in mind that different settings, e.g. the mesh, will affect the results. The results in this paper are from simulations where the solver settings are not the main limiting factor for the accuracy, but rather the representation of the antenna.

Two of the most important antenna quantities are installed far-field patterns and isolation between antennas [1]. The installed far-field patterns are of large importance when determining the functionality of a radio frequency (RF) system, which is determined e.g. by the coverage for a sensor installed on a vehicle. There can be a large difference between an antennas *isolated radiation pattern*, which is the radiation pattern for the antenna in free space, and its *installed radiation pattern*, which is the radiation pattern when installed on a platform. Hence, as is well known, antennas must be analyzed within their complete environment [33]. The isolation between antennas is related to the risk for interference between the antennas. It is an important quantity in antenna placement studies [1]. The isolation between antennas are mainly determined by direct propagating waves and surface currents, see e.g. [34]. The accuracy of surface currents is thus an important contribution to the accuracy of isolation between antennas, in particular for antennas without line-of-sight.

The following quantities are used for evaluating the accuracy of the results using the equivalent sources:

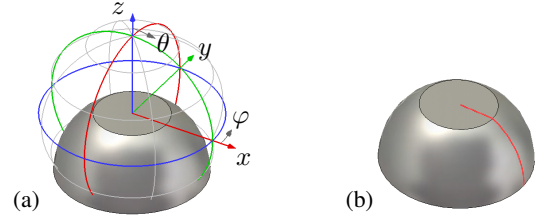- The electric current $\boldsymbol{J}$ along the red curve in Fig. 3(b).

Fig. 3. Definition of (a) the spherical angles θ and φ, and their relation to the Cartesian coordinates x, y, z, (b) the curve used for evaluation of currents. The curve is parametrized by the arc length ℓ, where $\ell = 0$ is the center of the flat top, and $\ell \approx 155$ mm is the periphery of the bottom of the geometry.

- The installed far-field $\boldsymbol{E}(\varphi, \theta)$ for all inclination angles $\theta = [0, 180°]$ and a fixed azimuth $\varphi = 90°$.

We use (1) to evaluate the current $\boldsymbol{J}$ based on the magnetic field $\boldsymbol{H}$. The magnetic field $\boldsymbol{H}$ can be separated into components parallel and orthogonal to the azimuthal unit vector $\hat{\mathbf{e}}_\varphi$,

$$H_\varphi = \hat{\mathbf{e}}_\varphi \cdot \boldsymbol{H}, \tag{3}$$
$$|H_{r,\theta}| = |\hat{\mathbf{e}}_\varphi \times \boldsymbol{H}|. \tag{4}$$

The propagating component H_φ is dominant outside the reactive region, so that $\boldsymbol{H} \approx H_\varphi \hat{\mathbf{e}}_\varphi$. With this approximation, the electric current $\boldsymbol{J}$ can be calculated as

$$\boldsymbol{J} = \hat{\mathbf{n}} \times \boldsymbol{H} \approx H_\varphi (\hat{\mathbf{n}} \times \hat{\mathbf{e}}_\varphi). \tag{5}$$

The rotational symmetry implies that $\hat{\mathbf{n}} \times \hat{\mathbf{e}}_\varphi = -\hat{\mathbf{e}}_t$, where $\hat{\mathbf{e}}_t$ is the outward pointing tangent unit vector along the curve in Fig. 3(b). The tangential current J_t along the curve is

$$J_t = \hat{\mathbf{e}}_t \cdot \boldsymbol{J} \approx -H_\varphi. \tag{6}$$

We denote the complex tangential current from the references solution $J_t^{\text{ref}}(\ell)$ and when using an equivalent source $J_t(\ell)$. The scalar ℓ is the arc length along the curve in Fig. 3(b). We define the relative magnitude error $\delta_{\text{rel}}|J_t(\ell)|$ and the phase error $\angle \delta J_t(\ell)$ of the complex current as

$$\delta_{\text{rel}}|J_t(\ell)| = \frac{|J_t(\ell)| - |J_t^{\text{ref}}(\ell)|}{|J_t^{\text{ref}}(\ell)|}, \tag{7}$$
$$\delta \angle J_t(\ell) = \angle J_t(\ell) - \angle J_t^{\text{ref}}(\ell), \tag{8}$$

where $\angle(\cdot)$ denotes the argument of a complex number.

When calculating the current J_t, by using (6), we evaluate H_φ a small distance $d > 0$ above the surface. The reason for this is numerical stability. The field $\boldsymbol{H}$ will be zero inside the PEC structure, and by setting $d > 0$ we assure that the evaluation points are not inside the structure. We use $d = 0.5$ mm, which is empirically determined to be the smallest distance for which all evaluation points fall outside the PEC.

The installed electric far-field $\boldsymbol{E}$ is separated into its components parallel and orthogonal to the azimuthal unit vector $\hat{\mathbf{e}}_\varphi$, so that

$$E_\varphi = \hat{\mathbf{e}}_\varphi \cdot \boldsymbol{E}, \tag{9}$$
$$|E_{r,\theta}| = |\hat{\mathbf{e}}_\varphi \times \boldsymbol{E}|. \tag{10}$$

Due to symmetry, $E_\varphi = 0$. On large distances from the antenna, the radial component vanishes, so that

$$\boldsymbol{E} \approx E_\theta \hat{\mathbf{e}}_\theta. \tag{11}$$

We denote the complex electric far-field component from the references solution $E_\theta^{\text{ref}}(\varphi,\theta)$, and when using an equivalent source $E_\theta(\varphi,\theta)$. From the electric far-fields $E_\theta^{\text{ref}}(\varphi,\theta)$ and $E_\theta(\varphi,\theta)$, we can evaluate both the magnitude error and the phase error. In this paper, we only evaluate the magnitude error of the installed far-field, which is the most commonly used quantity to classify installed antennas. The relative magnitude error $\delta_{\text{rel}}|E_\theta(\varphi,\theta)|$ is defined as

$$\delta_{\text{rel}}|E_\theta(\varphi,\theta)| = \frac{|E_\theta(\varphi,\theta)| - |E_\theta^{\text{ref}}(\varphi,\theta)|}{|E_\theta^{\text{ref}}(\varphi,\theta)|}. \quad (12)$$

By evaluating the far-field component E_θ, we will be able to see systematic errors, which would be hidden in the normalization if e.g. the directivity was evaluated.

Note that it is the field components H_φ and E_θ in their respective regions that are used as inputs to the benchmarks in (7)–(8) and (12). Hence, the approximations in (6) and (11) do not affect the accuracy of the benchmark[2]. The introduced notation, $\delta_{\text{rel}}|J_t(l)|$, $\delta\angle J_t(l)$ and $\delta_{\text{rel}}|E_\theta(\varphi,\theta)|$, is motivated by the physical relevance of these quantities.

D. Solvers and Simulation Settings

The equivalent sources are generated using FIT. In the evaluation of the equivalent sources, we examine their robustness, with respect to design parameters, by using them as excitations and solve in the full domain using FIT or MoM, as well as the asymptotic method Shooting-Bouncing-Rays (SBR). All simulations are performed using CST Microwave Studio (MWS) [11].

The frequency, 10 GHz, is chosen so that fields in the domain D_0 can be calculated with full-wave methods on a desktop computer. The size of the domains D_0 and D_1 is set so that they contain the structure of interest and $1.5\,\lambda$ of space on each side.

IV. RESULTS

A. The Reference Solution

In order to get reliable estimates of the accuracy, it is crucial to have a highly accurate reference solution with the model of the physical antenna, as in Fig 1. We verify that the solution is accurate by examining the variability of the results from three different numerical methods; Finite integration technique (FIT), Method of moments (MoM), Finite element method (FEM), see e.g. [5], [31], [32].

The magnitude of the tangential electrical current, $|J_t^{\text{ref}}(\ell)|$, along the line in Fig. 3(b), is depicted in Fig. 4. The currents calculated with different methods agree well, with a relative RMS difference between FIT and MoM currents of $3.4\,\%$. The difference between FIT and FEM is $9.3\,\%$ and between MoM and FEM it is $9.9\,\%$.

The installed far-field magnitude $|E_\theta^{\text{ref}}(\varphi,\theta)|$ is depicted in Fig. 5 for the azimuthal direction $\varphi = 90°$ and $\theta \in [0,180°]$. Again, the results from the numerical methods agree well, with a relative RMS difference between the far-fields calculated

[2]For a rotational symmetric problem, as in this case, the expressions (6) and (11) are exact.
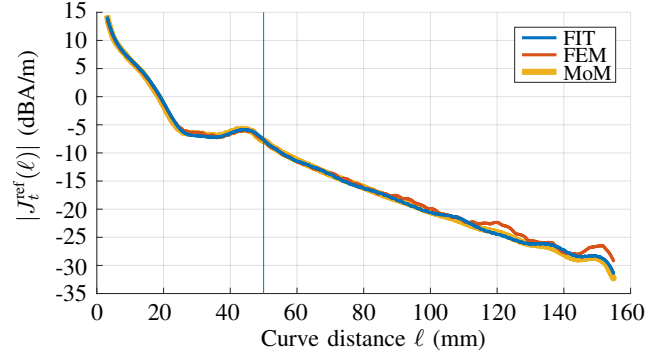

Fig. 4. Reference case: The current $|J_t^{\text{ref}}(\ell)|$ tangentially along the curve in Fig. 3(b), solved with three different numerical methods. The vertical line at $l = 50$ mm marks the edge of the flat top.
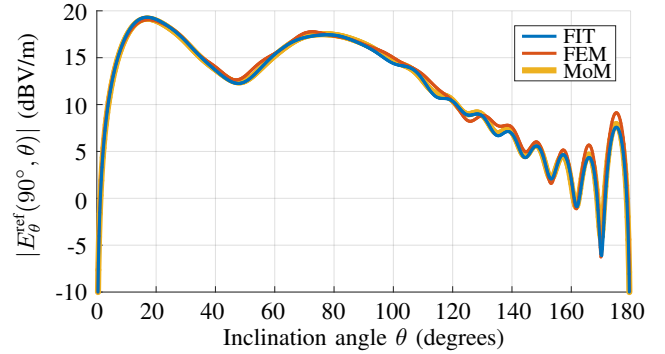

Fig. 5. Reference case: Installed electric far-field magnitude $|E_\theta^{\text{ref}}(90°,\theta)|$, solved with three different numerical methods.

with FIT and MoM of $3.1\,\%$. The difference between FIT and FEM is $7.4\,\%$ and between MoM and FEM it is $6.2\,\%$.

The agreement of the results from the different numerical methods indicate that the reference solutions are accurate. We see in Fig. 4 that the solutions using MoM and FIT conform best with the expected exponential decay of the current on the curved surface. Of these two solutions, with good mutual agreement, the FIT solution is chosen as the reference, since FIT is the native solver in CST MWS.

We can relate some of the properties seen in Fig. 4–5 to the platform. The slope of surface current in Fig. 4 for $\ell > 50$ mm depends on the curvature of the sphere. The double beam at $\theta \approx 17°$, $\theta \approx 78°$, and the local minimum between, of the installed far-field in Fig. 5 is an effect of the flat top surface of the platform. A smaller radius of the flat top would lift the beams, i.e. decrease the inclination angle θ. The oscillations for $\theta \in (100°,180°)$ in Fig. 5 are caused by reflections in the bottom edge of the platform G.

B. Results for the Near-field Source Configuration

The realization of near-field sources depend on the choice of the sub-domain D_1 and the placement of the surface Γ_e, see Fig. 2, but also on the choice of ground-plane geometry. The aim here is to evaluate the freedom of choice with respect to these geometrical parameters. We consider six different configurations of surfaces Γ_e and ground planes, as defined in Fig. 6, with dimensions given in Table I. The configurations evaluated are motivated briefly below.

TABLE I
DIMENSIONS OF SURFACES Γ_e FOR EVALUATED CONFIGURATIONS.

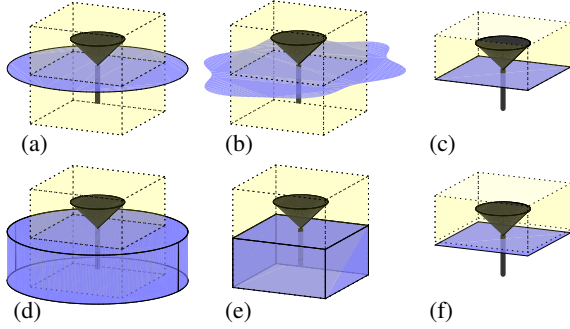| Conf.	x	y	z
NFS (a)	$|x| = 25$ mm	$|y| = 25$ mm	$|z| = 25$ mm
NFS (b)	$|x| = 25$ mm	$|y| = 25$ mm	$|z| = 25$ mm
NFS (c)	$|x| = 25$ mm	$|y| = 25$ mm	$z = 0$, $z = 25$ mm
NFS (d)	$|x| = 25$ mm	$|y| = 25$ mm	$|z| = 25$ mm
NFS (e)	$|x| = 25$ mm	$|y| = 25$ mm	$|z| = 25$ mm
NFS (f)	$|x| = 25$ mm	$|y| = 25$ mm	$z = 1$ mm, $z = 25$ mm

Fig. 6. The configurations of ground plane (blue) and surface Γ_e (yellow) when generating near-field sources; the ground-plane is (a) a thin 100 mm diameter PEC plate, (b) a thin infinite PEC plate, (c) and (f) a thin 50×50 mm^2 PEC plate, (d) a solid 100 mm diameter, 25 mm thick PEC plate, (e) the part of the structure G contained inside the interface Γ_e. Note that the bottom of the surface Γ_e coincide with the ground plane in (c), whereas it is 1 mm above the ground plane in (f).

Configuration (a) is generated with a thin sheet PEC plate and has non-zero currents also on the lower half of Γ_e, as can be seen in Fig. 7(a) and Fig. 8(a). The same applies to (e), because Γ_e coincide with the PEC boundary. The infinite ground plane in (b) is estimating the whole platform as a ground plane, whereas (a) and (d) account for the local geometry of the platform. The diameter of the circular PEC plate in configurations (a) and (d) is 100 mm (3.3λ) and corresponds to the diameter of the flat platform top, see Fig. 1.

Configurations (d) and (e) have with solid ground-planes, resulting in $90°$ edges on the ground plane. In the configurations (a), (c), and (f), the ground planes are thin sheets, resulting in sharp edges. In configuration (b), with an infinite ground-plane, there are no ground-planes discontinuities.

One of the key features in (a) and (d) is that they capture a larger part of the platform geometry as compared to the other configurations. Configurations (c), (e), (f) all take a ground plane with a side length 50 mm (1.7λ) that correspond to the horizontal size of the equivalent surface Γ_e. The effect caused by the currents on the ground plane can be observed by comparing (c) and (f), since the surface Γ_e coincide with the ground plane in (c) whereas it is 1 mm above the ground plane in (f). Note that the square ground plane in configurations (c), (e), (f) does not conform to the azimuthal symmetry of the original problem. However, the field solutions corresponding to configurations (c) and (e) show less asymmetry than (f), as can be seen in Fig. 8, possibly due to the effects of the ground plane that coincide with Γ_e in (c) and (e), but not in (f). An advantage of setting the ground-plane size equal to the size of the surface Γ_e, as in (c), (e), and (f), is that the sub-domain D_1 is minimal, leading to shorter simulation times.
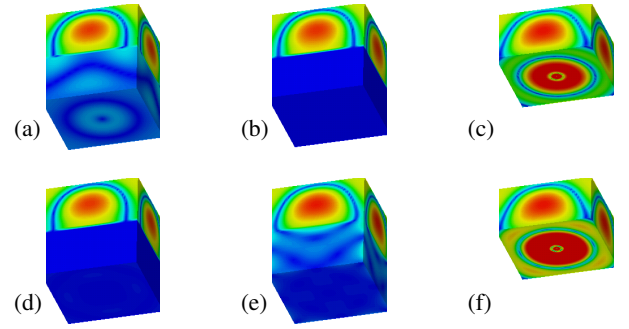

Fig. 7. Tangential magnetic field magnitudes $|\hat{\mathbf{n}} \times \boldsymbol{H}|$ on Γ_e for the configurations in Fig. 6. The logarithmic color scale ranges from 0 to 1 A/m.
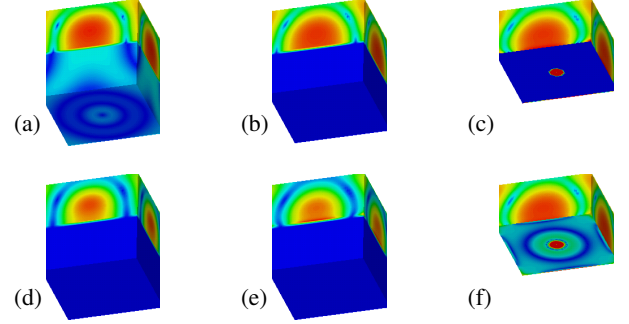

Fig. 8. Tangential electric field magnitudes $|\hat{\mathbf{n}} \times \boldsymbol{E}|$ on Γ_e for the configurations in Fig. 6. The logarithmic color scale ranges from 0 to 320 V/m.

TABLE II
ROOT-MEAN-SQUARE ERRORS USING NEAR-FIELD SOURCE AND FIT.

Configu- ration	RMS (linear scale)		
	$\delta_{\text{rel}}|J_t(\ell)|$, $\ell \in (25, 155]$ mm	$\delta\angle J_t(\ell)$, $\ell \in (25, 155]$ mm	$\delta_{\text{rel}}|E_\theta(90°,\theta)|$, $\theta \in (0, 180°)$
NFS (a)	10.1 %	4.8°	6.0 %
NFS (b)	8.2 %	5.9°	4.4 %
NFS (c)	9.2 %	7.1°	8.4 %
NFS (d)	9.3 %	5.0°	5.1 %
NFS (e)	9.7 %	6.9°	7.4 %
NFS (f)	8.9 %	5.7°	7.3 %

The work flow described in Section III-B1 is followed when generating and using the near-field sources. Since the reference solution was solved with FIT, we use FIT again to determine the fields with the near-field sources imprinted on the platform.

The resulting near-field source representations of the antenna are depicted in Fig. 7–8, for each of the configurations used. The strong fields on the bottom surface of (c) and (f) is due to the coaxial feed cable that penetrates the surface Γ_e.

The accuracy is evaluated by the tangential current errors $\delta_{\text{rel}}|J_t(\ell)|$ and $\delta\angle J_t(\ell)$, according to (7) and (8). They are presented in Table II as RMS errors and depicted in Fig. 9 for the interval $\ell \in (25, 155]$ mm, i.e. outside the equivalent surface Γ_e. The installed far-field errors $\delta_{\text{rel}}|E_\theta(90°,\theta)|$, according to (12), are depicted in Fig. 10 and the RMS errors for $\theta \in (0, 180°)$ are listed in Table II.

The behavior in terms of $\delta_{\text{rel}}|J_t(\ell)|$ RMS errors are similar in all configurations, with small variations in the relative error between 8.2 % and 10.1 %. A correct local geometry of the ground-planes, as in (a) and (d), is important for the accuracy of the surface currents close to the source. We see this clearly
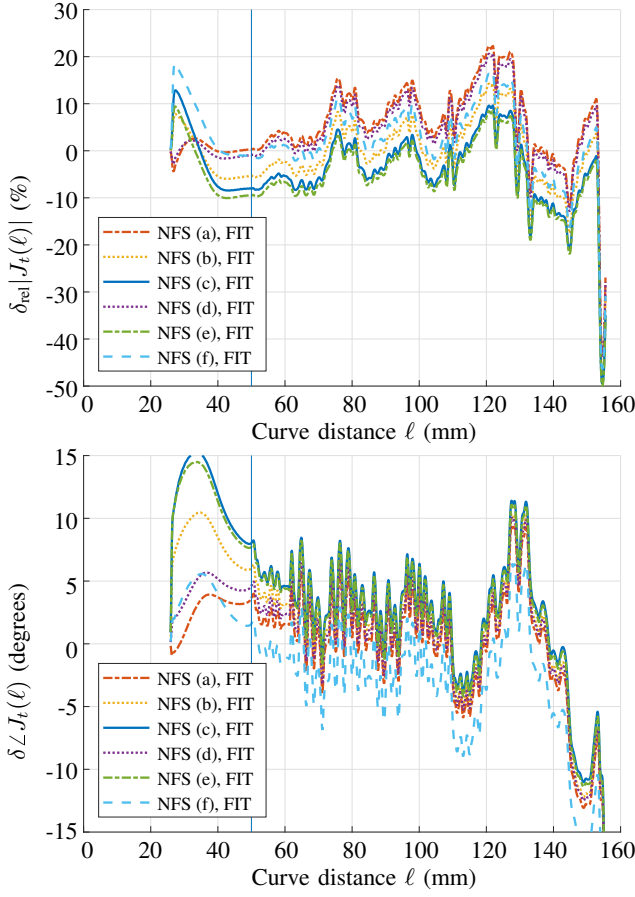
Fig. 9. The relative surface current magnitude error $\delta_{\mathrm{rel}}|J_t(\ell)|$ (top) and surface current phase error $\delta\angle J_t(\ell)$ (bottom), for different near-field source configurations, see Fig. 6. The errors are evaluated along the curve in Fig. 3(b). The vertical line at $\ell = 50$ mm marks the edge of the flat top of the geometry.
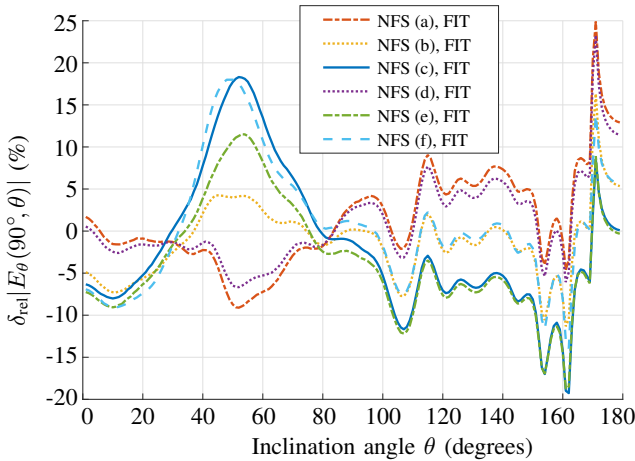

Fig. 10. Relative installed electric far-field errors $\delta_{\mathrm{rel}}|E_\theta(90°, \theta)|$ using the equivalent near-field sources illustrated in Fig. 6.

in Fig. 9(a) close to the equivalent source $\ell < 50$ mm.

For the installed far-field in Fig. 10, we see that the variation is smaller between the different configurations, as compared to the current error in Fig. 9. This is expected due to the smoothing effect for far-fields. The smallest RMS error $\delta_{\mathrm{rel}}|E_\theta(90°, \theta)|$ are for (b) with 4.4% and (d) with 5.1%, which are comparable with the variations of the reference

solutions on 3.1%. In Fig. 10, the difference between configuration is particularly large in the region $\theta \in [30°, 80°]$, motivating a closer study. The max-norm deviations in this region range from $4°$ with (b) to $18°$ with (c) and (f). We see that the edge of the ground-plane seems to play an important role for the accuracy in this region, where (b) performs best (no discontinuity), and the configuration with a square thin sheet ground-plane, (c) and (f), give the least accurate results. Comparing (a) and (d), we see that (d) with a solid ground-plane ($90°$ edge) is more accurate than (a) with a thin ground-plane (sharp edge). We see the same pattern when comparing (c) with (e); the solid ground-plane performs better than the thin sheet ground-plane with a sharp edge. The size of the ground plane also plays a role. A small ground plane gives a lifting effect of the pattern from the horizontal plane (as discussed in Sec. IV-A). The large errors for (c), (e), (f) is partly caused by this effect, where the beam maximum is shifted from $\theta \approx 78°$ to $\theta \approx 72°$. The computationally simple configuration (b) with an infinite ground-plane gives accurate results, especially for the installed far-fields.

The expected higher sensitivity of the currents as compared with the far-field is clearly observed in Table II. Compared with the estimated RMS uncertainty in the reference solutions in Section IV-A (3.4% for the current magnitude and 3.1% for the installed far-field magnitudes), we see in Table II that the near-field sources increase the current magnitude uncertainty with a factor of 2.4–5.6 and the far-field magnitude uncertainty with a factor of 1.4–2.7.

To conclude this section, we note that the RMS errors of the currents, is about 9% for the best case (see Table II), with max-norm deviations up to $\pm 20\%$ for $\ell \in (25, 150)$ mm, rising up to $\pm 50\%$ close to the bottom platform edge at $\ell = 155$ mm (see Fig. 9). Similarly, the phase has about $5°$ RMS error for the best configurations (see Table II), with max-norm deviation up to $\pm 15°$ (see Fig. 9). For the installed far-fields, we note that the RMS errors are about 5% for the best cases, with corresponding max-norm deviations up to $\pm 10\%$ over $\theta \in [0, 160°]$. We note that the RMS errors of the far-field vary with a factor of two between the most and least accurate configurations.

C. Results for Far-field Source Configuration

When generating the far-field sources, we consider three configurations, as defined in Fig. 11. From these configurations, we use FIT to calculate their far-field patterns. The results, which are used as far-field sources, are depicted in Fig. 12(a) for the vertical cut $\varphi = \pm 90°$ and Fig. 12(b) for the horizontal cut $\theta = 70°$. The inclination $\theta = 70°$ is depicted since the three far-field patterns have similar magnitude making it easy to compare the curves and identify asymmetries. Note that configuration (b), with an infinite ground plane, results in a far-field pattern that is identical to zero in the lower hemisphere, $\theta > 90°$. Configuration (c) will not preserve the symmetry in φ of the original problem, but the effect is small, as can be seen in Fig. 12(b).

The work flow described in Section III-B2 is used for generating and using the far-field sources. Because of the rotational
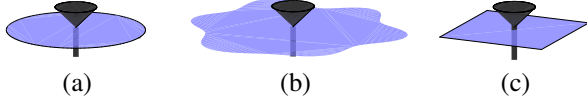
Fig. 11. The configurations of ground plane when generating far-field sources; (a) a 100 mm diameter PEC plate, (b) a infinite PEC plate, and (c) a 50 × 50 mm² PEC plate. All three plates are infinitesimally thin.
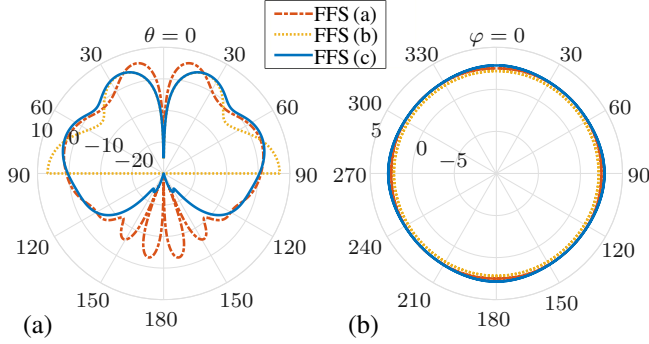

Fig. 12. Realized gain of far-field sources for the configurations illustrated in Fig. 11, for (a) azimuths $\varphi = \pm 90°$ and inclinations $\theta \in [0, 180°]$, and (b) azimuths $\varphi = \in [0, 180°]$ and inclination $\theta = 70°$.

symmetry of the platform geometry G, the far-field source is placed on the symmetry axis $x = 0$, $y = 0$. In contrast, the position h on the vertical axis is not trivial. Compared to e.g. a geometrical theory of diffraction (GTD) formulation [35], the source, in that case a dipole moment, can be placed both on the conducting surface or above it. We investigate four cases of the design parameter $h = (0, 2, 4, 10)$ mm, i.e. the distance above the flat platform top, see Fig. 2. The resulting problem is solved with MoM, since FIT in CST Microwave Studio [11] cannot handle far-field sources.

The accuracy of the far-field sources are evaluated with the current errors $\delta_{\mathrm{rel}}|J_t(\ell)|$ and $\delta\angle J_t(\ell)$, according to (7) and (8). These errors are depicted in Fig. 13 and listed as RMS errors in Table III for the investigated configurations. The far-field errors $\delta_{\mathrm{rel}}|E_\theta(\varphi, \theta)|$, according to (12), are depicted in Fig. 14.

The ground plane in (c) is smaller than the flat surface of G. Despite that, as depicted in Fig. 12, far-field source (c) radiates less in the lower hemisphere, as compared with (a) and (b). We note in Table III that the far-field error $\delta_{\mathrm{rel}}|E_\theta(\varphi, \theta)|$ is smallest with (c), especially for $\theta > 90°$. This is somewhat surprising, since (a) captures the local geometry of the platform better. However, the asymmetry of (c) makes it less attractive to use.

If (b) is installed on a height $h > 0$ mm, there are no fields impinging on the platform, resulting in zero currents on the platform and also zero field for $\theta > 90°$ (which is the reason for the omitted numbers in Table III). Hence, when generating a far-field source using an infinite ground plane, the resulting far-field source should be installed on the platform surface, i.e. $h = 0$. For the other far-field sources, i.e. (a) and (c), it is hard to give any recommendations for the value of h.

Compared with the estimated RMS uncertainty in the reference solutions in Section IV-A (3.4 % for the current magnitude and 3.1 % for the installed far-field magnitudes), we see in Table III that the far-field sources increase the current magnitude uncertainty by a factor of 11–48 and the far-field
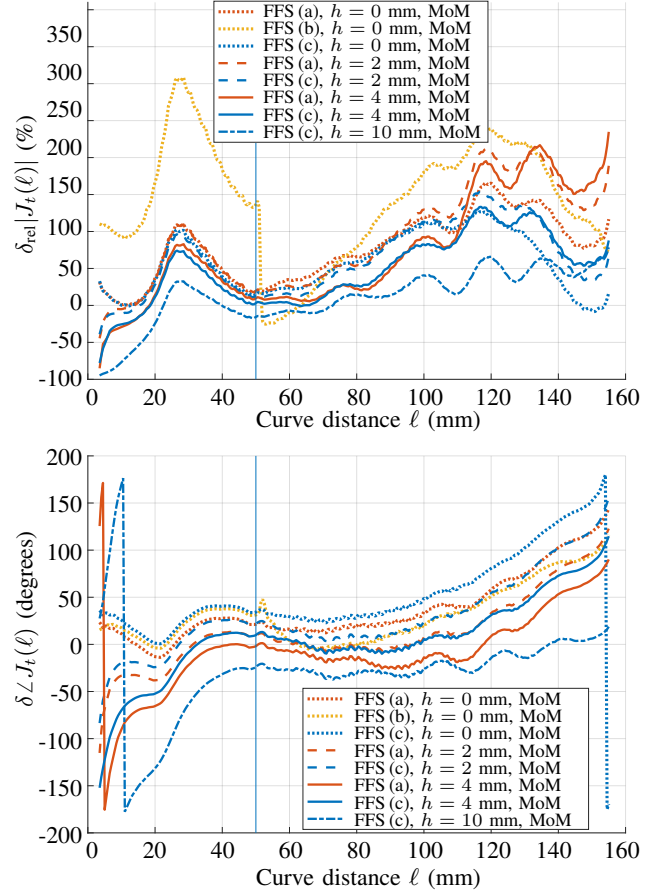

Fig. 13. The relative current magnitude errors $\delta_{\mathrm{rel}}|J_t(\ell)|$ (top) and current phase errors $\delta\angle J_t(\ell)$ (bottom) evaluated along the curve in Fig. 3(b) using the far-field sources in Fig. 11, installed on height h above the flat top of G.

TABLE III
ROOT-MEAN-SQUARE ERRORS USING FAR-FIELD SOURCE AND MoM.

Configu-ration	$h =$	RMS (linear scale)			
		$\delta_{\mathrm{rel}}|J_t(\ell)|$, $\ell \in$ (3, 155] mm	$\delta\angle J_t(\ell)$, $\ell \in$ (3, 155] mm	$\delta_{\mathrm{rel}}|E_\theta|$, $\theta \in$ (0, 180°)	$\delta_{\mathrm{rel}}|E_\theta|$, $\theta \in$ (0, 90°)
FFS (a)	0 mm	89 %	52°	133 %	44 %
FFS (b)		163 %	44°	77 %	57 %
FFS (c)		70 %	69°	46 %	41 %
FFS (a)	2 mm	112 %	40°	133 %	47 %
FFS (b)		–	–	74 %	27 %
FFS (c)		79 %	52°	54 %	41 %
FFS (a)	4 mm	105 %	45°	127 %	30 %
FFS (b)		–	–	74 %	27 %
FFS (c)		66 %	44°	45 %	14 %
FFS (a)	10 mm	61 %	61°	115 %	31 %
FFS (b)		–	–	74 %	27 %
FFS (c)		39 %	58°	40 %	25 %

magnitude uncertainty by a factor of 13–43 (for $\theta \in (0, 180°)$).

Since the near-field behavior is not captured with far-field sources, it is expected that the surface currents are inaccurate. It is notable, however, that also the installed far-fields depicted in Fig. 14 are more inaccurate, as compared to using NFS. It is also notable that the placement h of the far-field source has such a strong impact, see Fig. 13–14. Its influence is in same order of magnitude as the choice of configuration.
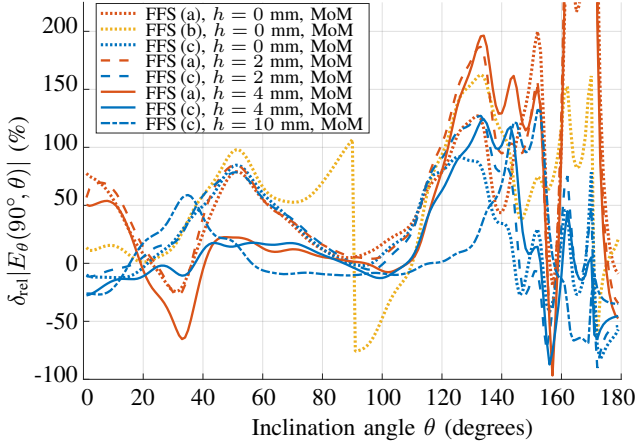
Fig. 14. The relative installed far-field errors $\delta_{\mathrm{rel}}|E_\theta(90°, \theta)|$ using the far-field sources in Fig. 11 installed on height h above the flat top of G.
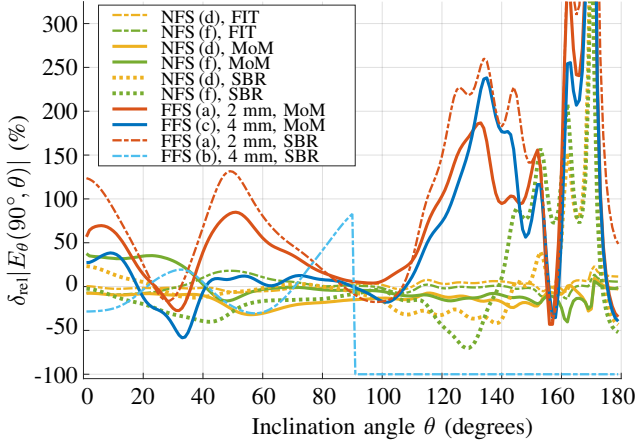

Fig. 15. The relative installed far-field errors $\delta_{\mathrm{rel}}|E_\theta(90°, \theta)|$ using three different numerical methods; FIT, MoM, and SBR.

D. Results on the Impact of the Numerical Method

The above discussed results evaluate the accuracy of two different types of equivalent antenna representations. To determine how the estimated accuracy depends on the choice of numerical method, we use the best near-field configurations, see Fig. 10, and the best far-field source, see Fig. 14, with different numerical methods. For near-field sources, we compare the accuracy of FIT with the accuracy of MoM and SBR. For the far-field sources we compare the accuracy of MoM with SBR. We do not consider FIT for far-field sources since it is not implemented in the current version of CST.

We use a subset of the equivalent sources from previous sections; three near-field sources; NFS (b) with best $\delta_{\mathrm{rel}}|E_\theta(90°, \theta)|$, NFS (d) with best $\delta_{\mathrm{rel}}|J_t(\ell)|$, and NFS (f) with best $\delta\angle J_t(\ell)$, and three far-field sources, FFS (a) $h = 2$ mm with best $\delta\angle J_t(\ell)$, FFS (c) $h = 4$ mm with best $\delta|E_\theta|$, and FFS (c) $h = 10$ mm with best $\delta_{\mathrm{rel}}|J_t(\ell)|$. The relative installed far-field errors $\delta_{\mathrm{rel}}|E_\theta(90°, \theta)|$, defined in (12), from these equivalent sources are calculated with different numerical methods, FIT, MoM, and SBR. The resulting errors are depicted in Fig. 15 and also listed as RMS errors in Table IV.

We see in Table IV that, when using near-field sources, FIT

TABLE IV
ROOT-MEAN-SQUARE ERRORS FOR DIFFERENT NUMERICAL METHODS AND EQUIVALENT SOURCES.

Configuration	RMS (linear scale)		
	$\delta_{\mathrm{rel}}|E_\theta(90°, \theta)|, \theta \in (0, 180°)$		
	FIT	MoM	SBR
NFS (b)	4.4 %	23 %	56 %
NFS (d)	5.1 %	16 %	57 %
NFS (f)	7.3 %	18 %	65 %
FFS (a), 2 mm	–	133 %	195 %
FFS (b), 4 mm	–	74 %	74 %
FFS (c), 4 mm	–	45 %	88 %
FFS (c), 10 mm	–	40 %	91 %

performs significantly better than MoM and SBR. On average, RMS errors are 3 times higher with MoM and 9 times higher with SBR, as compared with FIT.

When using far-field sources, MoM gives more accurate results than SBR, as seen in Table IV. None of the numerical methods give accurate results for $\theta > 90°$ with far-field sources, see Fig. 15. With the combination of FFS (b), $h > 0$ mm and SBR, there are no fields impinging on the platform, resulting in a zero field for $\theta > 90°$. In Fig. 15, it is clear that the near-field sources are an order of magnitude more accurate than the far-field sources. Similar effects are observed in the currents as seen by comparing Table II with Table III.

V. DISCUSSION AND CONCLUSIONS

Electromagnetic simulations of antennas installed on large platforms are challenging problems. The often complex antenna in combination with an electrically large platform leads to very high memory requirements and long simulation times. One way to reduce the complexity is to represent the antenna with an equivalent model that is more effective to use in simulations.

This paper presents one of the first accuracy studies of equivalent sources on platforms. The considered platform has weak backscattering and one installed antenna. Several different configurations has been considered, with respect to the approximation of the platform and geometrical parameters associated with the generation of the equivalent sources.

The determined deviations from the reference solution are presented for each of the examined configuration of the equivalent sources. The results give a first indication of errors associated with equivalent sources on a platform. Translating error levels to generic platforms are challenging, however, it is clear from the study that the platform associated backscattering is important for the accuracy of the equivalent representation.

In agreement with knowledge from using equivalent representations in homogeneous environments (i.e. not on platforms), near-field sources perform significantly better than far-field sources for all configurations considered. The near-field sources, in the presence of the considered weakly scattering platform, are comparably robust, with respect to location and size of the equivalent surface. The resulting RMS accuracies of the best cases evaluated are about 8% and $5°$ for the surface current magnitude and phase, respectively, and about 4% for the installed far-field magnitude.

The accuracy of the far-field sources with respect to surface current phase in the considered cases is rather low. In our opinion, far-field sources should not be used when current phase information is required. In the best case investigated, the installed far-field RMS error on the magnitude is about 31 % and for the current 23 %. The installed height above the platform of the far-field source has a strong effect on the accuracy, which introduce an uncertainty in the use of far-field sources. One should bear in mind that a far-field source, even though less accurate compared to a near-field source, is an efficient representation to use in numerical calculations. If the expected accuracy is within requirements, far-field sources can still be an attractive representation.

For the implementations in CST Microwave Studio, the most accurate results for the investigated platform are obtained when using near-field sources in combination with the full-wave solver FIT. With far-field sources, the accuracy is similar with MoM and SBR for directions within line-of-sight, whereas MoM performs better for non-line-of-sight directions.

References

[1] T. M. Macnamara, *Introduction to Antenna Placement and Installation*. John Wiley & Sons, 2010.

[2] EurAAP, "EurAAP Working Group on Software (WG4)," 2016.

[3] G. A. E. Vandenbosch and F. Mioc, "Bridging the simulations-measurements gap: State-of-the-art," in *2016 10th Eur. Conf. Antennas Propag.*, 2016.

[4] G. A. E. Vandenbosch, "Measurements and Simulations of the GSM Antenna," in *2016 10th Eur. Conf. Antennas Propag.*, Davos, 2016.

[5] T. Rylander, P. Ingelström, and A. Bondeson, *Computational Electromagnetics*, 2nd ed. Springer-Verlag New York, 2013, vol. 51.

[6] A. Toselli and O. Widlund, *Domain Decomposition Methods Algorithms and Theory*, 1st ed., ser. Springer Series in Computational Mathematics. Springer-Verlag Berlin Heidelberg, 2005.

[7] K. Zhao, V. Rawat, and J.-F. Lee, "A Domain Decomposition Method for Electromagnetic Radiation and Scattering Analysis of Multi-Target Problems," *IEEE Trans. Antennas Propag.*, vol. 56, no. 8, pp. 2211–2221, aug 2008.

[8] A. Becker and V. Hansen, "A hybrid method combining the Time-Domain Method of Moments, the Time-Domain Uniform Theory of Diffraction and the FDTD," *Adv. Radio Sci.*, vol. 5, no. 6, pp. 107–113, 2007.

[9] A. Barka and P. Caudrillier, "Domain Decomposition Method Based on Generalized Scattering Matrix for Installed Performance of Antennas on Aircraft," *IEEE Trans. Antennas Propag.*, vol. 55, no. 6 II, pp. 1833–1842, 2007.

[10] L. J. Foged, L. Scialacqua, F. Saccardi, F. Mioc, J. L. A. Quijano, and G. Vecchi, "Antenna placement based on accurate measured source representation and numerical tools," in *2015 IEEE Int. Symp. Antennas Propag. Usn. Natl. Radio Sci. Meet.*, 2015, pp. 1486–1487.

[11] CST, "Microwave Studio," 2016.

[12] Ansys, "HFSS," 2016.

[13] Altair, "FEKO," 2016.

[14] COMSOL, "COMSOL Multiphysics," 2016.

[15] T. Weiland, M. Timm, and I. Munteanu, "A Practical Guide to 3-D Simulation," *IEEE Microw. Mag.*, no. December, pp. 62–75, 2008.

[16] C. A. Balanis, "Antenna theory: a review," *Proc. IEEE*, vol. 80, no. 1, pp. 7–23, 1992.

[17] ——, *Antenna Theory Analysis and Design*, 3rd ed. John Wiley & Sons, 2005.

[18] L. J. Foged, L. Scialacqua, F. Saccardi, F. Mioc, D. Tallini, E. Leroux, U. Becker, J. L. Araque Quijano, and G. Vecchi, "Innovative representation of antenna measured sources for numerical simulations," in *IEEE Antennas Propag. Soc. AP-S Int. Symp.*, 2014, pp. 2014–2015.

[19] H. Wang, V. Khilkevich, Y. J. Zhang, and J. Fan, "Estimating radio-frequency interference to an antenna due to near-field coupling using decomposition method based on reciprocity," *IEEE Trans. Electromagn. Compat.*, vol. 55, no. 6, pp. 1125–1131, 2013.

[20] L. Li, J. Pan, C. Hwang, and J. Fan, "Radiation Noise Source Modeling and Application in Near-Field Coupling Estimation," *IEEE Trans. Electromagn. Compat.*, vol. 58, no. 4, pp. 1314–1321, 2016.

[21] N. Payet, M. Darces, J.-l. Montmagnon, M. Hélier, and F. Jangal, "Near field to far field transformation by using equivalent sources in HF band," in *15th Int. Symp. Antenna Technol. Appl. Electromagn.*, 2012, pp. 1–4.

[22] E. Tanjong, "Modeling the Installed Performance of Antennas in a Ship Topside Environment," CST, Tech. Rep., 2010.

[23] A. E. H. Love, "The Integration of the Equations of Propagation of Electric Waves," *Philos. Trans. R. Soc. London. Ser. A, Contain. Pap. a Math. or Phys. Character*, vol. 197, pp. 1–45, 1901.

[24] S. A. Schelkunoff, "Some Equivalence Theorems of Electromagnetics and Their Application to Radiation Problems," *Bell Syst. Tech. J.*, vol. 15, no. 1, pp. 92–112, 1936.

[25] W. L. Stutzman and G. A. Thiele, *Antenna Theory and Design*, 2nd ed. John Wiley & Sons, 1998.

[26] C. A. Balanis, *Antenna Theory: Analysis and Design*, 2nd ed. John Wiley & Sons, 1997.

[27] J. D. Jackson, *Classical Electrodynamics*, 3rd ed. John Wiley & Sons, Inc., 1999.

[28] A. D. Yaghjian, "Equivalence of surface current and aperture field integrations for reflector antennas," *IEEE Trans. Antennas Propag.*, vol. 32, no. 12, pp. 1355–1358, 1984.

[29] W. C. Gibson, *The Method of Moments in Electromagnetics*. Chapman & Hall/CRC, 2008.

[30] S. N. Makarov, *Antenna and EM Modeling with MATLAB*. John Wiley & Sons, 2002.

[31] A. Taflove and S. C. Hagness, *Computational Electrodynamics: The Finite-Difference Time-Domain Method*, 2nd ed. Artech House, 2000.

[32] W. C. Chew, J.-M. Jin, E. Michielssen, and J. Song, *Fast and Efficient Algorithms in Computational Electromagnetics*, ser. Antennas and Propagation Library. Artech House, 2001.

[33] B. L. Lepvrier, R. Loison, R. Gillard, L. Patier, P. Potier, and P. Pouliguen, "Analysis of Surrounded Antennas Mounted on Large and Complex Structures Using a Hybrid Method," in *8th Eur. Conf. Antennas Propag.*, 2014, pp. 2352–2355.

[34] J. Malmström, H. Frid, and B. L. G. Jonsson, "Approximate Methods to Determine the Isolation between Antennas on Vehicles," in *2016 IEEE Antennas Propag. Soc. Int. Symp.*, 2016, pp. 131–132.

[35] P. H. Pathak and N. Wang, "Ray analysis of mutual coupling between antennas on a convex surface," *IEEE Trans. Antennas Propag.*, vol. 29, no. 6, pp. 911–922, nov 1981.

Johan Malmström received the M.Sc. degree and Licentiate degree in electrical engineering from KTH Royal Institute of Technology, Stockholm, Sweden, in 2003 and 2017, respectively. He has been in industry working with electromagnetic calculations since 2004 and is currently with Saab, Surveillance, Stockholm, Sweden. During 2014–2017, he was a graduate student at the Electromagnetic Engineering Laboratory, KTH Royal Institute of Technology, within the area of computational electromagnetics and electromagnetic theory. His research was supported by Saab.

Henrik Holter received the M.Sc. degree in electrical engineering (with the distinction "Best Graduate of the Year") and the Ph.D. degree in electromagnetic theory from KTH Royal Institute of Technology, Stockholm, Sweden, in 1996 and 2000, respectively. He is currently at Saab, Electronic Warfare division, Stockholm, Sweden, where he is head of Research & Technologies. He has authored over 35 journal and conference publications in the area of array antennas. Dr. Holter was the recipient of the IEEE Antennas and Propagation Society 2003 R. W. P. King Award.

B. L. G. Jonsson received the Ph.D. degree in electromagnetic theory in 2001 from KTH Royal Institute of Technology, Stockholm, Sweden. He was a postdoctoral fellow at University of Toronto, Canada and a Wissenschaftlicher Mitarbeiter (postdoc) at ETH Zürich, Switzerland. Since 2006 he is with the Electromagnetic Engineering Laboratory at KTH where he is professor since 2015. His research interests include electromagnetic theory in a wide sense, including scattering, antenna theory and non-linear dynamics.